coatings

MDPI

Article

Tuning Nucleation Sites to Enable Monolayer Perovskite Films for Highly Efficient Perovskite Solar Cells

Yan Li [1,2], Xiaolei Li [2], Qianqian Chu [2], Hui Dong [1,2], JiantaoYao [1,2], Yong Zhou [1] and Guanjun Yang [2,*]

[1] School of Materials Science and Engineering, Xi'an Shiyou University, Xi'an 710065, China; yli@xsyu.edu.cn (Y.L.); donghuihyy@163.com (H.D.); Jiantaoyao@xsyu.edu.cn (J.Y.); yzhou@xsyu.edu.cn (Y.Z.)

[2] State Key Laboratory for Mechanical Behavior of Materials, School of Materials Science and Engineering, Xi'an Jiaotong University, Xi'an 710049, China; lixiaoleimse@sina.com (X.L.); Cqqonly@163.com (Q.C.)

* Correspondence: ygj@mail.xjtu.edu.cn; Tel.: +86-29-826-65299

Received: 27 September 2018; Accepted: 16 November 2018; Published: 18 November 2018

Abstract: The nucleation site plays a critical role in achieving the full coverage of perovskite film at both the macroscopic and microscopic scales, and it is systematically investigated for the first time in this study. The results show that under natural conditions, the incomplete coverage of perovskite film is due to both heterogeneous nucleation and homogeneous nucleation. The established concentration field and temperature field in the precursor solution show that there are two preferential nucleation sites, i.e., the upper surface of the precursor solution (homogeneous nucleation) and the surface of the substrate (heterogeneous nucleation). The nucleation sites are tuned by decreasing the drying pressure from the atmosphere to 3000 Pa, and then to 100 Pa, and then the microstructures of the perovskite films change from an incomplete coverage state to a monolayer full coverage state, and then to a bilayer full coverage state. At last, when the full coverage perovskite films are assembled into perovskite solar cells, the photovoltaic performance of the monolayer perovskite solar cells is slightly greater than that of the bilayer perovskite solar cells. The electrochemical characterization shows that there is more restrained internal recombination of the monolayer perovskite solar cells compared with bilayer perovskite solar cells.

Keywords: nucleation site; crystallization; perovskite film; full coverage; microstructure

1. Introduction

Ever since the first evidence emerged that hybrid organic-inorganic lead halide perovskites should be a candidate for high performance photovoltaic devices, strong research effort has been mainly divided into two directions: Improving the conversion efficiency [1,2] and enhancing environmental stability [3,4]. For perovskite solar cells (PSCs) with planar configuration, which are low cost and more suitable for industrialization, both the high conversion efficiency and high environmental stability strongly depend on the full coverage state of the perovskite film (PVK) at both macroscopic and microscopic scales on the substrate [5,6]. Until now, many approaches have been attempted to realize the scalable full coverage perovskite film [7–9]. Considering the one-step solution fabrication process is a promising method for the preparation of perovskite film, due to its easy operation, low cost, and no reverse reaction [10,11], a number of approaches have been explored to control the steps that link the initial precursors to the final perovskite film during the solution fabrication process.

Regarding the preparation process, replacing precursor species [12,13], manipulating the ratio of precursors [14–16], adding additives in the precursor solution [17–19], treating the substrate surface [20,21], as well as enhancing solvent evaporation [22,23], have been proved to be efficient approaches to increase the coverage ratio or even to realize the full coverage state of the perovskite films, and the various correlations between the microstructures of the perovskite films and their photovoltaic performance have been established. Due to the promising results, the underlying scientific issues of the solution fabrication process, related to the correlation between crystallization behavior (supersaturation, nucleation and growth up) attract a lot of attention of the researchers. Previous results have showed that tuning the nucleation and growth up behavior of the perovskite is an efficient procedure to control the microstructure of the perovskite film [20,24–26]. For example, Bi et al. [20] and Kim et al. [24] changed the surface energy of the hole transport layer to manipulate the heterogeneous nucleation, and the enlarged perovskite grains were prepared for the high performance PSCs. Ren et al. [26] proposed a temperature-assisted rapid nucleation method to realize fast crystallization of perovskite film, and they thought the growth of homogeneous nuclei would result in a dense perovskite film. In addition, by manipulating the competition between nucleation and growth [27] and by restraining the overgrowth of localized crystals [28], the coverage ratio of the perovskite film could be improved. In all, it is important to effectively control and optimize the coverage ratio of the perovskite film through the guidance of crystallization crystallography, which has been widely proved to be an efficient way of manipulating the microstructures of crystals [29–32].

To prepare the full coverage state of the perovskite film on both the macroscopic and microscopic scales, firstly, the nuclei should appear at the rough substrate surface; secondly, they should grow up not only along the out-plane direction (perpendicular to the apparent substrate surface), but also along the in-plane direction (parallel to apparent substrate surface); at lastly, the perovskite crystals should contact each other in a crosswise direction and subsequently, grow up only in the out-plane direction [33]. The uniform, close-packed, columnar crystal microstructure is benefit for sufficient light absorption [34], as it restrains internal recombination [35] and decreases contact with water/oxygen [36]. Considering the nucleation is the original step of the crystallization process, therefore, it is desirable to investigate the nucleation behavior which is one of the most important components of crystallography in the solution fabrication process of perovskite film.

In this study, to investigate the nucleation behavior in perovskite precursor solution, the surface morphologies and cross-sectional views of the perovskite films prepared under natural drying conditions are systematical characterized, and it is surprisingly found that the incomplete coverage perovskite film is formed by both heterogeneous and homogeneous nucleation. To establish the fundamental physics from the nucleation site to the full coverage state at both macroscopic and microscopic scales, the temperature field and concentration field of the precursor solution are analyzed, and it is shown there are two separate preferential nucleation sites at the surface of precursor solution and the surface of the substrate. By tuning the nucleation sites, the perovskite films change from incomplete coverage to monolayer full coverage, and then to bilayer full coverage. At last, when both full coverage films are assembled into solar cells, the photovoltaic performance of the monolayer perovskite solar cells is slightly greater than bilayer perovskite solar cells.

2. Materials and Methods

2.1. Precursor and Perovskite Film Preparation

Lead iodide (PbI_2, reagent grade) and methylammonium iodide (ICH_3NH_3, reagent grade) purchased from Xi'an Polymer Light Technology Corp. (Xi'an, China) were used as the solute. N,N-dimethylformamide (DMF, reagent grade) purchased from Sigma-Aldrich (Darmstadt, Germany) was used as the solvent. Transparent fluorine-doped tin oxide (FTO, TEC-15, LOF) conductive glasses were cut into 25 × 25 mm^2 portions, and were employed as substrates. Before perovskite film deposition, the substrates were cleaned in ultrasonic acetone and an alcohol bath, and then they were dried using high purity nitrogen gas.

For preparation of the precursor solution, equal stoichiometric amounts of PbI_2 and ICH_3NH_3 were dissolved in DMF under magnetic stirrer to form a 30 wt.% solution, and then kept at 70 °C for more than 5 h. For preparation of the perovskite film, firstly, the precursor solution was dropped on FTO and spin-coated at 4000 rpm for 10 s, and during the process the redundant solution had been flung off leaving solution of non-fluidity; secondly, the samples were dried under atmospheric pressure or rapidly transferred to a chamber and then dried by the gas pumping method [37], and during the process the solute became perovskite crystals through supersaturation, nucleation and the growth step. The whole gas pumping process only needed less than 1 min, and all the processes were carried out in atmosphere. To restrain the evaporation of the DMF before the second step, the laboratory temperature was kept below 25 °C.

2.2. Perovskite Solar Cell Fabrication

A TiO_2 compact layer was deposited on the FTO substrate (TiO_2/FTO substrate), and the TiO_2 compact layer precursor was purchased from Xi'an Polymer Light Technology Corp. (Xi'an, China). Then, the perovskite film was deposited on the TiO_2/FTO substrate as shown in the illustration in Section 2.1. After the as-prepared film had been annealed at 100 °C for 0.5 h, the hole transport layer (HTM) was deposited by spin-coating at 3000 rpm for 30 s, where the HTM solution consisted of 80 mg spiro-OMeTAD (2,2′,7,7′-tetrakis(N,N-di-p- methoxyphenylamine)-9,9′-spirobifluorene), 28.5 μL 4-tert-butylpyridine and 17.5 μL lithium-bis(trifluoromethanesulfonyl) imide (Li-TFSI) solution (520 mg Li-TFSI in 1 mL acetonitrile) and 1 mL chlorobenzene. The HTM was purchased from Xi'an Polymer Light Technology Corp. (Xi'an, China). Finally, a 200 nm thick Au layer was deposited on the HTM layer by thermal evaporation.

2.3. Characterization

The surface morphologies and sectional views of the $CH_3NH_3PbI_3$ films were characterized by field emission scanning electron microscopy (FESEM, TESCAN, Brno, Czech Republic). The X-ray diffraction (XRD) patterns of perovskite films and FTO substrate were characterized with an X-ray diffractometer (SHIMADZU, Kyoto, Japan) with Cu Kα radiation. The content of elements in the ultra-thin perovskite layer was determined by energy dispersive X-ray spectroscopy (EDS, Oxford, UK). The performances of the solar cells were measured by a solar simulator (100 $mW \cdot cm^{-2}$, Oriel 94023 A, Newport) equipped with a Keithley 2400 digital source meter (Tektronix, San Francisco, CA, USA). The cells were measured in an area of 0.10 cm^2 under sunlight. The electrochemical impedance spectroscopy (EIS) was measured using an electrochemical workstation (IM6, ZAHNER, Kansas City, MO, USA) under illumination with an amplitude of 20 mV and a frequency range of 10^{-1} to 10^6 Hz.

3. Results and Discussion

3.1. Nucleation Behavior of the Perovskite Precursor under Natural Drying Conditions

According to the one-step solution method, under natural drying conditions, perovskite films can be simply prepared through three steps: Dropping the precursor solution on the substrate, spin-coating to get an ideal liquid film thickness, and subsequently drying to remove all the solution naturally. It can be seen in Figure 1a that under natural drying conditions, at the macroscopic level, the perovskite film shows a dendritic structure leaving a large fraction of incompletely covered areas surrounded by the dendritic structures, as illustrated in previous literature [38,39]. However, through careful observation, it can be seen that the tail ends of the dendritic structures appear to overlap, which are indicated by red arrows in Figure 1a. When we put one of the tails ends in a high magnification (as shown in Figure 1b), it is found that the tail ends of the dendritic structures stack together, indicating there are multilayer perovskite films there; this is indicated by the red dotted circle. Furthermore, based on Figure 1b, in addition to the obvious dendritic structure, there seems to be an ultra-thin layer of perovskite film appearing in the incompletely covered areas, and one demonstration area is indicated with a blue dotted rectangle in Figure 1b. When it is in a higher magnification, the thin perovskite film is clearer (Figure 1c), and only a fraction of the incompletely

covered area is really the bare substrate surface, and the other areas are actually covered with the ultra-thin layer of perovskite film. The EDS result shows that it contains Pb and I in a ratio close to 1:3 (Figure 1d). What we do not know yet is whether it is heterogeneous nucleation because it is too thin to be found in the cross-sectional view. However, we speculate that the ultra-thin perovskite film comes from pure heterogeneous nucleation.

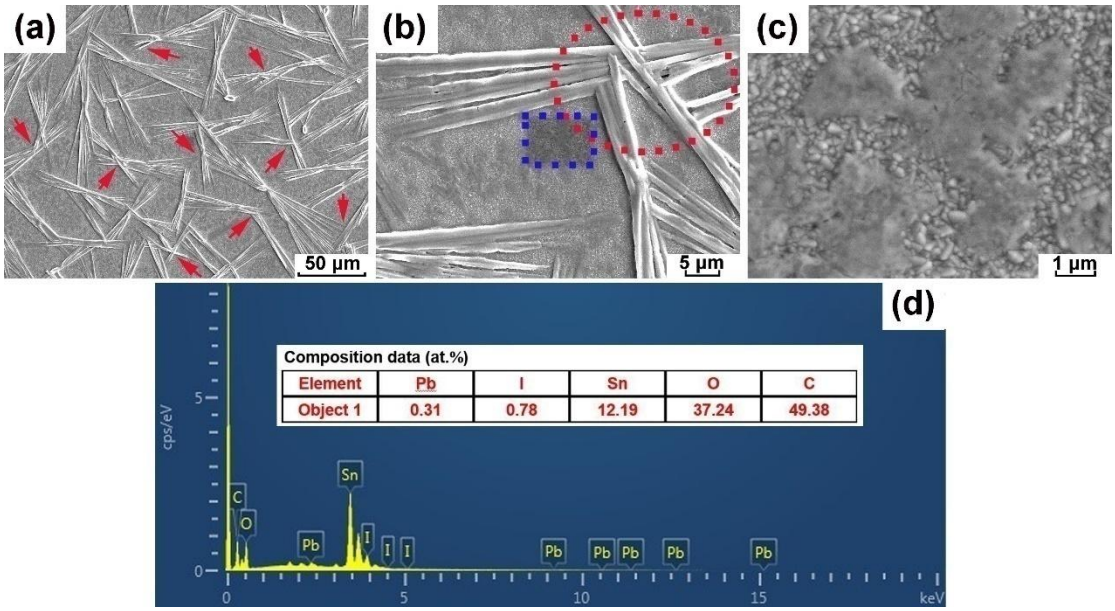

Figure 1. The surface morphologies of the perovskite film prepared under natural drying conditions: (**a**) Low magnification and (**b**) high magnification. (**c**) The surface morphology of the ultra-thin perovskite film indicated with blue dotted rectangle in (**b**). (**d**) The chemical composition of the ultra-thin perovskite film in (**c**).

The typical cross-sectional views of the perovskite film under natural drying conditions are also shown in Figure 2. There is not only a monolayer perovskite area, as shown in Figure 2a, but also a bilayer perovskite area, as shown in Figure 2b. We know that when the solution is under supersaturation, nucleation behavior is the original step for the crystallization process. The crystals grow up based on the nuclei. Therefore, based on the bilayer perovskite morphology, it can be deduced that there is surely homogeneous nucleation in the precursor solution. Further, it can also be deduced that under natural drying conditions, the final dendritic perovskite film is formed by crystals coming from both heterogeneous nucleation and homogeneous nucleation. Considering the unstrained supersaturation state under natural drying condition, there will be limited heterogeneous nuclei and homogeneous nuclei appearing in the precursor solution, and then based on the long solvent evaporation time, indicating long crystal growth time, there is more and more solute accumulated localized leaving the other areas having no enough solute to grow up. Therefore, there are incomplete coverage areas in the substrate.

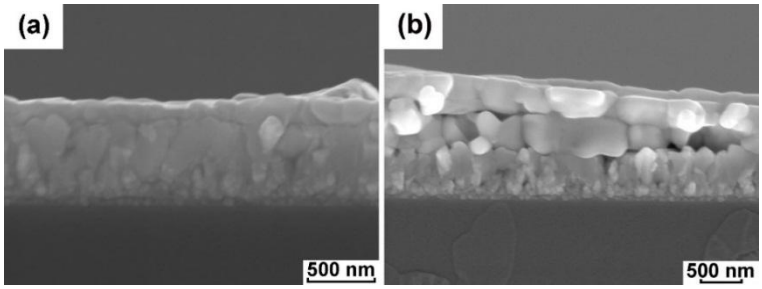

Figure 2. The typical cross-sectional views of the perovskite film under natural drying conditions: (**a**) The monolayer perovskite area; and (**b**) the bilayer perovskite area.

3.2. Correlation between Nucleation Sites and Microstructures of Perovskite Films

The nucleation site is the original critical factor in achieving the full coverage of perovskite film on both the macroscopic and microscopic scales; therefore, in order to clearly understand the nucleation behavior of the perovskite precursor under any condition, the mass and heat transfer processes in the precursor solution was investigated. The thickness for the precursor solution left on the substrate after spin-coating is 3.1 μm (Figure 3a), which was calculated by measuring the solution weight, indicating measuring the weight difference between bare FTO and the precursor/FTO after spin-coating. The whole measuring process was less than 1 min, and the ambient temperature was kept below 25 °C. Both are to restrain the inaccuracy caused by evaporation of the DMF. The precursor solution thickness is much smaller than the length of the upper surface (25 mm); therefore, the evaporation from the lateral surface of the precursor solution after spin-coating can be ignored.

After spin-coating, the evaporation of the upper surface results in solute accumulation there; then, there is a decline in the concentration field from the upper surface to the substrate surface, and Figure 3b is the schematic diagram of the concentration field. Furthermore, the experimental results by us show that the evaporation of the DMF is a heat absorption process, which reduces the temperature of the upper surface, and then, there is a temperature field decline from the upper surface to the substrate surface. Figure 3c is the schematic diagram of concentration field. As the solubility of $CH_3NH_3PbI_3$ in DMF decreases as the temperature decreases [40], if appropriate supersaturation is provided by the concentration field and temperature field, the upper surface of the precursor solution becomes one of the preferential sites for nucleation. The other preferential nucleation site is at the substrate surface because the energy barrier for heterogeneous nucleation is lower than that of the homogeneous nucleation (Figure 3d).

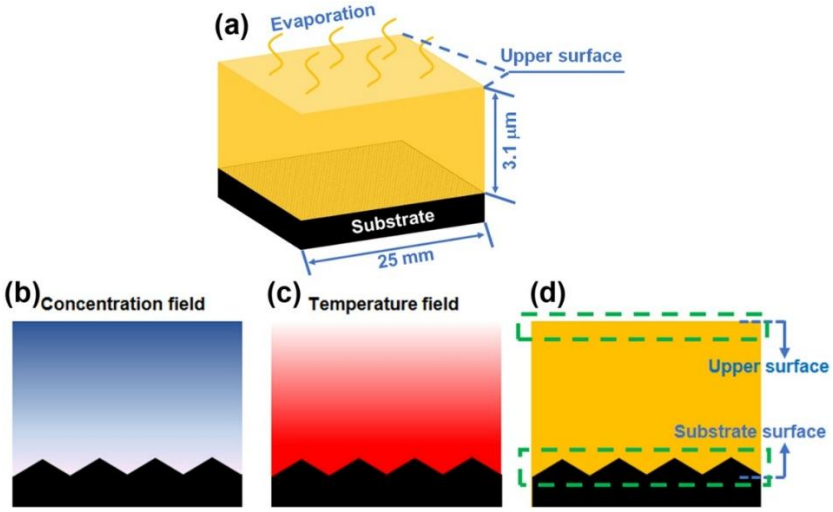

Figure 3. Schematic diagrams of the boundary conditions for the precursor solution (**a**), concentration field (**b**), temperature field (**c**), and the possible preferential nucleation sites marked with the green dotted box in the precursor solution film during evaporation (**d**).

For the confined space (3.1 μm for the thickness of precursor solution), convection, which is a powerful method for homogenizing both the concentration and temperature fields, is impossible [41,42]. Therefore, the temperature and concentration homogenization processes depend on the thermal transmission and solute diffusion, separately. On one hand, the greater enhancement of solvent evaporation leads to more serious solute accumulation and temperature decline at the upper surface, which increases the supersaturation state at the upper surface (homogeneous nucleation). On the other hand, a more serious solute accumulation and temperature decline leads to greater enhancement of thermal transmission and solute diffusion from the upper surface to the substrate surface, which enhances heterogeneous nucleation and its growth. Therefore, there is a competitive relationship between the homogeneous nucleation (upper surface) and heterogeneous nucleation (substrate surface).

Under natural drying conditions, the weak evaporation of the solvent yields the unstrained competitive relationship between homogeneous nucleation and heterogeneous nucleation; therefore, the free nucleation tendency results in incompletely covered areas, monolayer perovskite areas, and bilayer perovskite areas coexisting. To enhance solvent evaporation, the low-pressure method was chosen as a demonstration, and the drying pressure to the perovskite precursor solution was decreased from atmospheric pressure to 3000 Pa, and then to 100 Pa. The surface morphologies of perovskite films changed from an incomplete coverage state to monolayer full coverage perovskite film, and then to bilayer full coverage perovskite film, which are shown in Figure 4a,b, and it can be seen that both show an apparent full coverage state based on their surface morphologies.

The corresponding cross-sectional views of both films are shown in Figure 4c,d. As shown in Figure 4c, when the drying pressure is decreased to 3000 Pa, the perovskite film is monolayer. Based on the surface morphology and cross-sectional view of it, it can be deduced that it is in a full coverage state on both macroscopic and microscopic scales. We know that the energy barrier for heterogeneous nucleation is lower than that of homogeneous nucleation, therefore, the heterogeneous nucleation and growth under 3000 Pa can effectively relieve the supersaturation state of the whole precursor solution. When the drying pressure is decreased to 100 Pa, the two preferential nucleation sites result in the perovskite film showing a bilayer morphology (Figure 4d), which illustrates that the thermal transmission and solution diffusion process under 100 Pa cannot effectively relieve the solute accumulation at the upper surface of the precursor solution. Based on Figure 4c,d, the thickness of bilayer perovskite film seems a little thicker than the monolayer perovskite film, which can be attributed to the non-uniform internal crystal stacking state which may introduce some voids in the bilayer perovskite film.

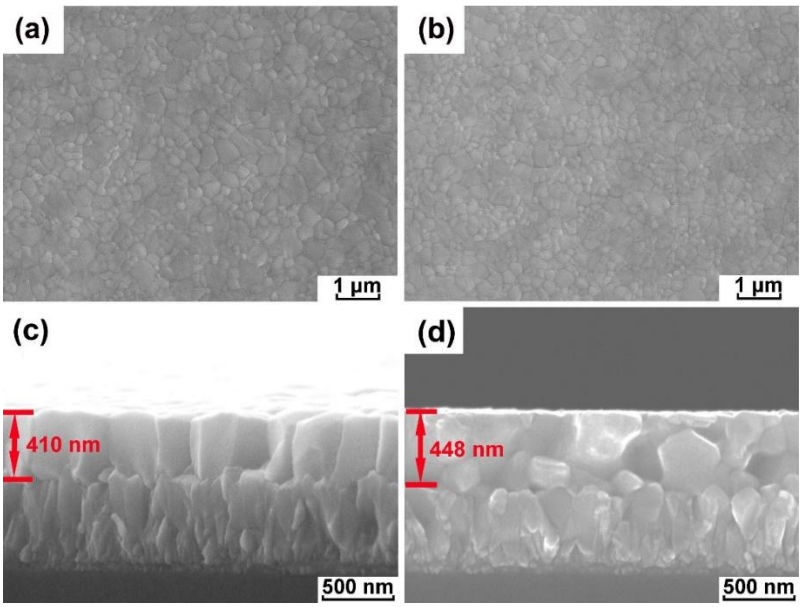

Figure 4. The surface morphologies of the perovskite films: (**a**) Monolayer prepared under 3000 Pa and (**b**) bilayer prepared under 100 Pa. The cross-sectional views of the perovskite films: (**c**) Monolayer prepared under 3000 Pa and (**d**) bilayer prepared under 100 Pa.

In addition to the possible preferential nucleation sites, the appearance of the nuclei inside the precursor solution is also possible under conditions of the ultra-high supersaturation which is provided by ultra-fast solvent evaporation. When the drying pressure is decreased to 10 Pa, the perovskite film is stacked with a lot of particles that form a multilayer morphology based on the cross-sectional view of the perovskite film shown in Figure S1. Under this situation, the drying pressure is too low, which makes the solvent evaporation too fast, and then the serious amount of solute accumulated in the precursor solution does not have enough time to homogenize by diffusion, therefore, it precipitates in situ.

3.3. Photovoltaic Performance of the Perovskite Solar Cells

The full coverage perovskite films on either scale was assembled into perovskite solar cells. The *J-V* curves for the typical solar cells are shown in Figure 5a, and the detailed data is listed in Table 1. It exhibited the performance with J_{sc} = 20.78 mA·cm^{-2}, V_{oc} = 1.09 V, FF = 71.74% and η = 16.25% for the monolayer PSCs, and J_{sc} = 20.10 mA·cm^{-2}, V_{oc} = 1.09 V, FF = 64.99% and η = 14.24% for the bilayer PSCs, where J_{sc} is the short-circuit density, V_{oc} is the open-circuit voltage, FF is the fill fact, and η is the conversion efficiency. In addition, more monolayer PSCs and bilayer PSCs were analyzed, and the results of the distribution of photovoltaic parameters are summarized in Figure 5b,e. The histogram format of the photovoltaic performances has been added as Figure S2 in the Supplementary Materials, and the detailed data has also been listed in Tables S1 and S2 of the supplementary materials. The V_{oc} of both solar cells are comparable, and the other parameters, including J_{sc}, FF and η for bilayer PSCs are a little lower than monolayer PSCs. Furthermore, it can be seen that there is a more serious discrete distribution of the J_{sc}, FF and η for bilayer PSCs compared with monolayer PSCs. The champion conversion efficiency is 19.14% for monolayer PSC, which is higher than the results of the PSCs with the same configuration of FTO/c-TiO_2/$CH_3NH_3PbI_3$/spiro-OMeTAD/Au reported in the last two years [43–50]. The weaker performance of the bilayer PSCs has been analyzed in the following section.

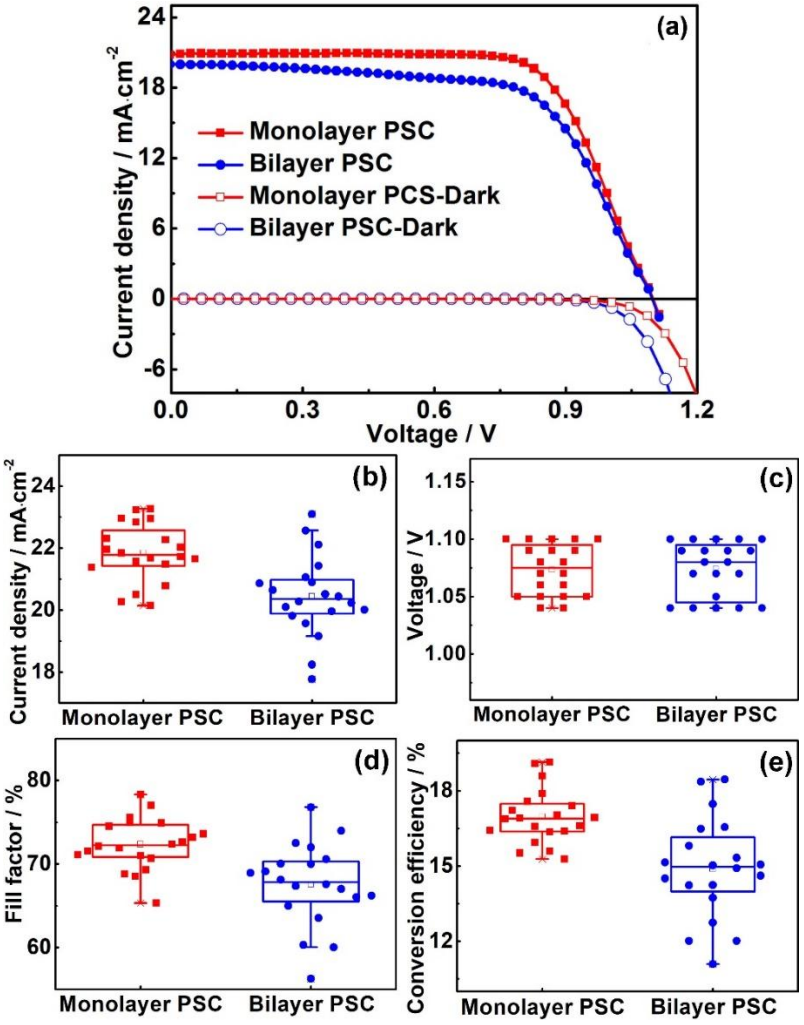

Figure 5. Typical photovoltaic performance of monolayer perovskite solar cells (monolayer PSCs) and bilayer perovskite solar cells (bilayer PSCs) obtained from reverse scanning under illumination and dark conditions (**a**). Statistical results of the photovoltaic parameters of monolayer PSCs and bilayer PSCs: J_{sc} (short-circuit density) (**b**), V_{oc} (open-circuit voltage) (**c**), FF (fill factor) (**d**) and η (conversion efficiency) (**e**).

Table 1. The detailed data of the typical photovoltaic performances of monolayer PSCs and bilayer PSCs in Figure 5a.

Cell type	J_{sc}/mA·cm^{-2}	V_{oc}/V	FF/%	η/%	τ_r/ms
Monolayer PSCs	20.78	1.09	71.74	16.25	0.45
Bilayer PSCs	20.10	1.09	64.99	14.24	0.19

To understand the slightly lower performance of bilayer PSCs compared with monolayer PSCs, the dark currents of both cells were characterized. As shown in Figure 5a, the monolayer PSCs exhibited a slightly lower dark current compared with the bilayer PSCs, which indicated suppressed charge recombination in the former. To further characterize the charge recombination in both solar cells, the EIS was proposed. The experimental results and fitting results are shown in Figure 6a, and the equivalent circuit is shown in the inset of Figure 6a. In the equivalent circuit, R_s is the series resistance of the whole cell. R_{ce} and C_{ce} correspond to the transport resistance and capacitance in the counter electrode, and the R_{ct} and C_{ct} correspond to the recombination resistance and capacitance of the perovskite film [51,52]. Based on the fitting results, the R_s of monolayer PSC is 2.78 Ω·cm^2, and the R_s of bilayer PSC is 5.03 Ω·cm^2. The R_{ce} of monolayer PSC is 117.3 Ω·cm^2, and the R_{ce} of bilayer PSC is 112.7 Ω·cm^2. The R_s and R_{ce} for both cells are comparable, however, the R_{ct} of monolayer PSC (346.0 Ω·cm^2) is larger than the bilayer PSC (278.5 Ω·cm^2), which is in accordance with the dark current results. The charge lifetime (τ_r) in the perovskite film was also estimated based on the bode phase plots in Figure 6b using the equation of $\tau_r = 1/(2\pi f_{max})$, where f_{max} corresponds to the frequency peak of the left intermediate frequency semicircle [53,54]. The calculated results are shown in Table 1, and the τ_r of the monolayer PSCs is shown to be a little longer than that of the bilayer PSCs.

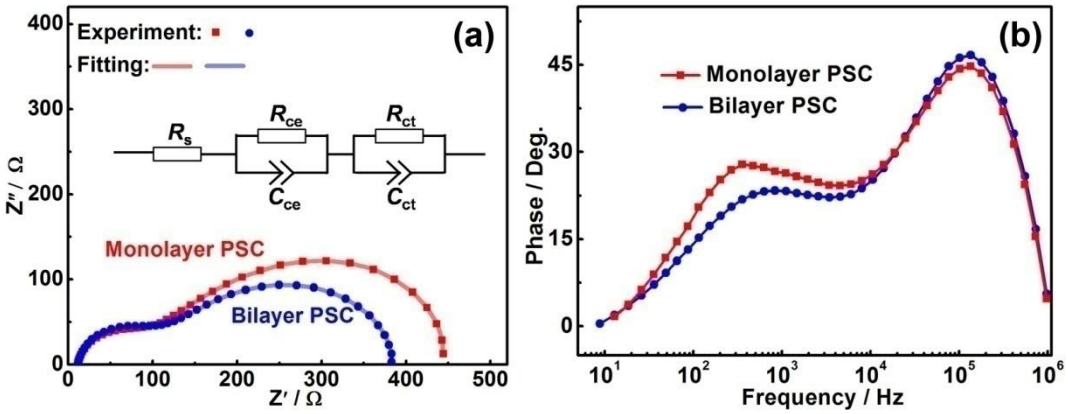

Figure 6. The electrochemical impedance spectroscopy (EIS) results of both solar cells characterized under open circuit voltage: (**a**) Nyquist plots and (**b**) bode phase plots. The equivalent circuit model to fit the EIS results is shown in inset of (**a**).

Based on the same assembly technology and characterization condition, the only difference between both solar cells is the microstructure of the perovskite film. Based on both heterogeneous nucleation and homogeneous nucleation, perovskite film is a layered structure with a number of grain boundaries, which is harmful for exciton transportation. At last the bilayer PSCs show a higher dark current, an enhanced internal recombination, and a short charge life time. The preferred type of perovskite film is the monolayer structure, i.e., grown up by heterogeneous nucleation to form the perovskite film on both the macroscopic and microscopic scales. This is beneficial for the perovskite film/substrate contact, and extends the exciton's lifetime and even isolates oxygen/water. Much effort will be paid to nuclei behavior control in future, to allow improvements in the conversion efficiency and industrialization of the perovskite solar cells.

4. Conclusions

Manipulation of the crystallization process is important for optimizing perovskite film microstructures during the solution preparation process. The nucleation site of the perovskite during the solution fabrication process was, first, systematically investigated. Through comprehensively analyzing the microstructures of the perovskite films prepared under natural drying conditions, it was found that the perovskite film contains incomplete covered areas, monolayer perovskite areas and bilayer perovskite areas. To explain this, schematic diagrams of the concentration field and temperature field were established based on the physical processes in the precursor solution. The results showed that there were two possible preferential nucleation sites: The upper surface of the precursor solution and the substrate surface. Then, the nucleation sites were manipulated by decreasing the drying pressure, and it was found that the microstructures of the perovskite films changed from incomplete coverage to a monolayer, and then to a bilayer. At last, both full coverage perovskite films were assembled into perovskite solar cells, and the characterization results showed that the conversion efficiency of the monolayer perovskite solar cells was slightly higher than bilayer perovskite solar cells for the restrained internal recombination. The investigation results provide insight into the crystallization control of perovskite film, which will aid in the industrialization of perovskite solar cells.

Supplementary Materials: The following are available online at https://www.mdpi.com/2079-6412/8/11/408/s1, Figure S1: The cross-sectional view of the perovskite film under the drying pressure of 10 Pa; Figure S2: Histogram format of the photovoltaic performance for both PSCs; Table S1: Photovoltaic performance of the monolayer PSCs; Table S2: Photovoltaic performance of the bilayer PSCs.

Author Contributions: Conceptualization, Y.L. and G.Y.; Methodology, Y.L., X.L. and Q.C.; Investigation, X.L. and Q.C.; Data Curation, H.D. and J.Y.; Writing—Original Draft Preparation, Y.L.; Writing—Review and Editing, Y.L., Y.Z. and G.Y.; Supervision, Y.Z. and G.Y.

Funding: The work was supported by the National Program for Support of Top-notch Young Professionals. National Science Foundation Research Project of Shaanxi Province (No. 2017JQ5042).

Conflicts of Interest: The authors declare no conflict of interest.

References

1. Jeon, N.J.; Na, H.; Jung, E.H.; Yang, T.-Y.; Lee, Y.G.; Kim, G.; Shin, H.-W.; Il Seok, S.; Lee, J.; Seo, J. A fluorene-terminated hole-transporting material for highly efficient and stable perovskite solar cells. *Nat. Energy* **2018**, *3*, 682–689.
2. Singh, T.; Miyasaka, T. Stabilizing the efficiency beyond 20% with a mixed cation perovskite solar cell fabricated in ambient air under controlled humidity. *Adv. Energy Mater.* **2018**, *8*, 1700677.
3. Niu, G.D.; Guo, X.D.; Wang, L.D. Review of recent progress in chemical stability of perovskite solar cells. *J. Mater. Chem. A* **2015**, *3*, 8970–8980.
4. Leijtens, T.; Eperon, G.E.; Noel, N.K.; Habisreutinger, S.N.; Petrozza, A.; Snaith, H.J. Stability of metal halide perovskite solar cells. *Adv. Energy Mater.* **2015**, *5*, 1500963.
5. Ye, J.; Liu, G.; Jiang, L.; Zheng, H.; Zhu, L.; Zhang, X.; Wang, H.; Pan, X.; Dai, S. Crack-free perovskite layers for high performance and reproducible devices via improved control of ambient conditions during fabrication. *Appl. Surf. Sci.* **2017**, *407*, 427–433.
6. Qiu, W.; Merckx, T.; Jaysankar, M.; de la Huerta, C.M.; Rakocevic, L.; Zhang, W.; Paetzold, U.W.; Gehlhaar, R.; Froyen, L.; Poortmans, J.; et al. Pinhole-free perovskite films for efficient solar modules. *Energy Environ. Sci.* **2016**, *9*, 484–489.
7. Gong, X.; Li, M.; Shi, X.B.; Ma, H.; Wang, Z.K.; Liao, L.S. Controllable perovskite crystallization by water additive for high-performance solar cells. *Adv. Funct. Mater.* **2015**, *25*, 6671–6678.
8. Das, S.; Yang, B.; Gu, G.; Joshi, P.C.; Ivanov, I.N.; Rouleau, C.M.; Aytug, T.; Geohegan, D.B.; Xiao, K. High-Performance Flexible Perovskite Solar Cells by Using a Combination of Ultrasonic Spray-Coating and Low Thermal Budget Photonic Curing. *ACS Photonics* **2015**, *2*, 680–686.

9. Xu, H.T.; Wu, Y.L.; Xu, F.Z.; Zhu, J.B.; Ni, C.W.; Wang, W.Z.; Hong, F.; Xu, R.; Xu, F.; Huang, J.; et al. Grain growth study of perovskite thin films prepared by flash evaporation and its effect on solar cell performance. *RSC Adv.* **2016**, *6*, 48851–48857.
10. Du, T.; Wang, N.; Chen, H.J.; Lin, H.; He, H.C. Comparative study of vapor- and solution-crystallized perovskite for planar heterojunction solar cells. *ACS Appl. Mater. Interfaces* **2015**, *7*, 3382–3388.
11. Chen, G.; Zheng, J.; Zheng, L.; Yan, X.; Lin, H.; Zhang, F. Crack-free $CH_3NH_3PbI_3$ layer via continuous dripping method for high-performance mesoporous perovskite solar cells. *Appl. Surf. Sci.* **2017**, *392*, 960–965.
12. Wang, F.; Yu, H.; Xu, H.H.; Zhao, N. A newprecursor compound for highly efficient solution-processed perovskite solar cells. *Adv. Funct. Mater.* **2015**, *25*, 1120–1126.
13. Li, C.; Guo, Q.; Qiao, W.Y.; Chen, Q.; Ma, S.; Pan, X.; Wang, F.Z.; Yao, J.X.; Zhang, C.F.; Xiao, M.; et al. Efficient lead acetate sourced planar heterojunction perovskite solar cells with enhanced substrate coverage via one-step spin-coating. *Org. Electron.* **2016**, *33*, 194–200.
14. Park, B.-S.; Lee, S.; Yoon, S.; Ha, T.-J.; Kang, D.-W. Methylammonium lead mixed halide films processed with a new composition for planar perovskite solar cells. *Appl. Surf. Sci.* **2018**, *427*, 421–426.
15. Yan, J.; Ke, X.; Chen, Y.; Zhang, A.; Zhang, B. Effect of modulating the molar ratio of organic to inorganic content on morphology, optical absorption and photoluminescence of perovskite $CH_3NH_3PbBr_3$ films. *Appl. Surf. Sci.* **2015**, *351*, 1191–1196.
16. Liu, D.; Liu, C.; Wu, L.L.; Li, W.; Chen, F.; Xiao, B.Q.; Zhang, J.Q.; Feng, L.H. Highly reproducible perovskite solar cells with excellent $CH_3NH_3PbI_{3-x}Cl_x$ film morphology fabricated via high precursor concentration. *RSC Adv.* **2016**, *6*, 51279–51285.
17. Zhang, L.; Yu, F.; Chen, L.; Li, J. Adsorption of molecular additive onto lead halide perovskite surfaces: A computational study on Lewis base thiophene additive passivation. *Appl. Surf. Sci.* **2018**, *443*, 176–183.
18. Song, X.; Wang, W.W.; Sun, P.; Ma, W.L.; Chen, Z.K. Additive to regulate the perovskite crystal film growth in planar heterojunction solar cells. *Appl. Phys. Lett.* **2015**, *106*, 033901.
19. Ding, Y.L.; Yao, X.; Zhang, X.D.; Wei, C.C.; Zhao, Y. Surfactant enhanced surface coverage of $CH_3NH_3PbI_{3-x}Cl_x$ perovskite for highly efficient mesoscopic solar cells. *J. Power Sources* **2014**, *272*, 351–355.
20. Bi, C.; Wang, Q.; Shao, Y.C.; Yuan, Y.B.; Xiao, Z.G.; Huang, J.S. Non-wetting surface-driven high-aspect-ratio crystalline grain growth for efficient hybrid perovskite solar cells. *Nat. Commun.* **2015**, *6*, 7747.
21. Cojocaru, L.; Uchida, S.; Sanehira, Y.; Nakazaki, J.; Kubo, T.; Segawa, H. Surface treatment of the compact TiO_2 layer for efficient planar heterojunction perovskite solar cells. *Chem. Lett.* **2015**, *44*, 674–676.
22. Xu, Q.Y.; Yuan, D.X.; Mu, H.R.; Femi, I.; Bao, Q.; Liao, L.S. Efficiency enhancement of perovskite solar cells by pumping away the solvent of precursor film before annealing. *Nanoscale Res. Lett.* **2016**, *11*, 248.
23. Huang, F.Z.; Dkhissi, Y.; Huang, W.C.; Xiao, M.D.; Benesperi, I.; Rubanov, S.; Zhu, Y.; Lin, X.F.; Jiang, L.C.; Zhou, Y.C.; et al. Gas-assisted preparation of lead iodide perovskite films consisting of a monolayer of single crystalline grains for high efficiency planar solar cells. *Nano Energy* **2014**, *10*, 10–18.
24. Kim, J.H.; Williams, S.T.; Cho, N.; Chueh, C.-C.; Jen, A.K.Y. Enhanced environmental stability of planar heterojunction perovskite solar cells based on blade-coating. *Adv. Energy Mater.* **2015**, *5*, 1401229.
25. Lewis, A.E.; Zhang, Y.; Gao, P.; Nazeeruddin, M.K. Unveiling the concentration-dependent grain growth of perovskite films from one- and two-step deposition methods: implications for photovoltaic application. *ACS Appl. Mater. Interfaces* **2017**, *9*, 25063–25066.
26. Ren, Y.-K.; Ding, X.-H.; Wu, Y.-H.; Zhu, J.; Hayat, T.; Alsaedi, A.; Xu, Y.-F.; Li, Z.-Q.; Yang, S.-F.; Dai, S.-Y. Temperature-assisted rapid nucleation: a facile method to optimize the film morphology for perovskite solar cells. *J. Mater. Chem. A* **2017**, *5*, 20327–20333.
27. Yang, G.J.; Ding, B.; Li, Y.; Huang, S.Y.; Chu, Q.Q.; Li, C.; Li, C. Material nucleation/growth competition tuning towards highly reproducible planar perovskite solar cells with efficiency exceeding 20%. *J. Mater. Chem. A* **2017**, *5*, 6840–6848.
28. Li, Y.; He, X.L.; Ding, B.; Gao, L.L.; Yang, G.J.; Li, C.X.; Li, C.J. Realizing full coverage of perovskite film on substrate surface during solution processing: Characterization and elimination of uncovered surface. *J. Power Sources* **2016**, *320*, 204–211.
29. Arefpour, A.; Shams Soolari, L.; Monshi, A. Improving mold powder through crystallization using calcium fluoride and manganese oxide for continuous casting of steel. *J. Adv. Ceram.* **2014**, *3*, 43–48.
30. Gautam, C.R.; Madheshiya, A.; Mazumder, R. Preparation, crystallization, microstructure and dielectric properties of lead bismuth titanate borosilicate glass ceramics. *J. Adv. Ceram.* **2014**, *3*, 194–206.

31. Li, J.; Ba, G.; Qi, X.; Li, X.; Song, Y.; Li, B. Nanocrystalline $BaTi_2O_5$ dielectric ceramic prepared by full crystallization from containerless solidified glass. *J. Adv. Ceram.* **2016**, *5*, 77–83.
32. Zhang, C.; Hu, D.; Gu, H.; Xing, J.; Xiong, P.; Wan, D.; Gao, Y. Crystallization and inter-diffusional behaviors in the formation of VO_2(B) thin film with layered W-doping. *J. Adv. Ceram.* **2017**, *6*, 196–206.
33. Li, Y.; Ding, B.; Chu, Q.Q.; Yang, G.J.; Wang, M.; Li, C.X.; Li, C.J. Ultra-high open-circuit voltage of perovskite solar cells induced by nucleation thermodynamics on rough substrates. *Sci. Rep.* **2017**, *7*, 46141.
34. Li, F.M.; Zhu, W.D.; Bao, C.X.; Yu, T.; Wang, Y.Q.; Zhou, X.X.; Zou, Z.G. Laser-assisted crystallization of $CH_3NH_3PbI_3$ films for efficient perovskite solar cells with a high open-circuit voltage. *Chem. Commun.* **2016**, *52*, 5394–5397.
35. Shen, Q.; Ogomi, Y.; Chang, J.; Tsukamoto, S.; Kukihara, K.; Oshima, T.; Osada, N.; Yoshino, K.; Katayama, K.; Toyoda, T.; et al. Charge transfer and recombination at the metal oxide/$CH_3NH_3PbClI_2$/spiro-OMeTAD interfaces: Uncovering the detailed mechanism behind high efficiency solar cells. *Phys. Chem. Chem. Phys.* **2014**, *16*, 19984–19992.
36. Bao, X.; Wang, Y.; Zhu, Q.; Wang, N.; Zhu, D.; Wang, J.; Yang, A.; Yang, R. Efficient planar perovskite solar cells with large fill factor and excellent stability. *J. Power Sources* **2015**, *297*, 53–58.
37. Ding, B.; Gao, L.; Liang, L.; Chu, Q.; Song, X.; Li, Y.; Yang, G.; Fan, B.; Wang, M.; Li, C. Facile and scalable fabrication of highly efficient lead iodide perovskite thin-film solar cells in air using gas pump method. *ACS Appl. Mater. Interfaces* **2016**, *8*, 20067.
38. Hsu, H.L.; Chen, C.P.; Chang, J.Y.; Yu, Y.Y.; Shen, Y.K. Two-step thermal annealing improves the morphology of spin-coated films for highly efficient perovskite hybrid photovoltaics. *Nanoscale* **2014**, *6*, 10281–10288.
39. Barrows, A.T.; Pearson, A.J.; Kwak, C.K.; Dunbar, A.D.F.; Buckley, A.R.; Lidzey, D.G. Efficient planar heterojunction mixed-halide perovskite solar cells deposited via spray-deposition. *Energy Environ. Sci.* **2014**, *7*, 2944–2950.
40. Heo, J.H.; Song, D.H.; Im, S.H. Planar $CH_3NH_3PbBr_3$ Hybrid Solar Cells with 10.4% Power Conversion Efficiency, Fabricated by Controlled Crystallization in the Spin-Coating Process. *Adv. Mater.* **2014**, *26*, 8179–8183.
41. Thomas, J.K.; Mathew, C.T.; Koshy, J.; Solomon, S. Influence of La^{3+} ion in the yttria matrix in improving the microhardness of infrared transparent nano $La_xY_{2-x}O_3$ sintered via hybrid heating. *J. Adv. Ceram.* **2017**, *6*, 240–250.
42. Clyne, T.W.; Golosnoy, I.O.; Tan, J.C.; Markaki, A.E. Porous materials for thermal management under extreme conditions. *Philos. Trans. A Math Phys. Eng. Sci.* **2006**, *364*, 125–146. DOI: 10.1098/rsta.2005.1682.
43. Che, M.; Fang, Y.; Yuan, J.; Zhu, Y.; Liu, Q.; Song, J. F-doped TiO_2 compact film for high-efficient perovskite solar cells. *Int. J. Electrochem. Sci.* **2017**, *12*, 1064–1074.
44. Chen, J.; Wan, Z.; Liu, J.; Fu, S.-Q.; Zhang, F.; Yang, S.; Tao, S.; Wang, M.; Chen, C. Growth of compact $CH_3NH_3PbI_3$ thin films governed by the crystallization in PbI_2 matrix for efficient planar perovskite solar cells. *ACS Appl. Mater. Interfaces* **2018**, *10*, 8649–8658.
45. Liang, C.; Li, P.; Zhang, Y.; Gu, H.; Cai, Q.; Liu, X.; Wang, J.; Wen, H.; Shao, G. Mild solution-processed metal-doped TiO_2 compact layers for hysteresis-less and performance-enhanced perovskite solar cells. *J. Power Sources* **2017**, *372*, 235–244.
46. Rajmohan, G.D.; Huang, F.Z.; d'Agostino, R.; du Plessis, J.; Dai, X.J. Low temperature reactively sputtered crystalline TiO_2 thin film as effective blocking layer for perovskite solar cells. *Thin Solid Films* **2017**, *636*, 307–313.
47. Ren, Z.; Zhu, M.; Li, X.; Dong, C. An isopropanol-assisted fabrication strategy of pinhole-free perovskite films in air for efficient and stable planar perovskite solar cells. *J. Power Sources* **2017**, *363*, 317–326.
48. Ye, T.; Xing, J.; Petrovic, M.; Chen, S.; Chellappan, V.; Subramanian, G.S.; Sum, T.C.; Liu, B.; Xiong, Q.; Ramakrishna, S. Temperature effect of the compact TiO_2 layer in planar perovskite solar cells: An interfacial electrical, optical and carrier mobility study. *Sol. Energy Mater. Sol. Cells* **2017**, *163*, 242–249.
49. Zardetto, V.; Di Giacomo, F.; Lifka, H.; Verheijen, M.A.; Weijtens, C.H.L.; Black, L.E.; Veenstra, S.; Kessels, W.M.M.; Andriessen, R.; Creatore, M. Surface fluorination of ALD TiO_2 electron transport layer for efficient planar perovskite solar cells. *Adv. Mater. Interfaces* **2018**, *5*, 1701456.
50. Zardetto, V.; Di Giacomo, F.; Lucarelli, G.; Kessels, W.M.M.; Brown, T.M.; Creatore, M. Plasma-assisted atomic layer deposition of TiO_2 compact layers for flexible mesostructured perovskite solar cells. *Sol. Energy* **2017**, *150*, 447–453.

51. Liu, D.Y.; Yang, J.L.; Kelly, T.L. Compact layer free perovskite solar cells with 13.5% efficiency. *J. Am. Chem. Soc.* **2014**, *136*, 17116–17122.
52. Song, J.X.; Zheng, E.Q.; Wang, X.F.; Tian, W.J.; Miyasaka, T. Low-temperature-processed ZnO-SnO_2 nanocomposite for efficient planar perovskite solar cells. *Sol. Energy Mater. Sol. Cells* **2016**, *144*, 623–630.
53. Adachi, M.; Sakamoto, M.; Jiu, J.T.; Ogata, Y.; Isoda, S. Determination of parameters of electron transport in dye-sensitized solar cells using electrochemical impedance spectroscopy. *J. Phys. Chem. B* **2006**, *110*, 13872–13880.
54. Bisquert, J.; Fabregat-Santiago, F.; Mora-Sero, I.; Garcia-Belmonte, G.; Gimenez, S. Electron lifetime in dye-sensitized solar cells: Theory and interpretation of measurements. *J. Phys. Chem. C* **2009**, *113*, 17278–17290.